

Input Convex Lipschitz RNN: A Fast and Robust Approach for Engineering Tasks

Zihao Wang^a, Zhe Wu^{*,a,b}

^a*Department of Chemical and Biomolecular Engineering, National University of Singapore, 117585, Singapore*

^b*Artificial Intelligence Institute, National University of Singapore, 117585, Singapore*

Abstract

Computational efficiency and robustness are essential in process modeling, optimization, and control for real-world engineering applications. While neural network-based approaches have gained significant attention in recent years, conventional neural networks often fail to address these two critical aspects simultaneously or even independently. Inspired by natural physical systems and established literature, input convex architectures are known to enhance computational efficiency in optimization tasks, whereas Lipschitz-constrained architectures improve robustness. However, combining these properties within a single model requires careful review, as inappropriate methods for enforcing one property can undermine the other. To overcome this, we introduce a novel network architecture, termed Input Convex Lipschitz Recurrent Neural Networks (ICLRNNs). This architecture seamlessly integrates the benefits of convexity and Lipschitz continuity, enabling fast and robust neural network-based modeling and optimization. The ICLRNN outperforms existing recurrent units in both computational efficiency and robustness. Additionally, it has been successfully applied to practical engineering scenarios, such as modeling and control of chemical process and the modeling and real-world solar irradiance prediction for solar PV system planning at LHT Holdings in Singapore.

Key words: Input Convex Neural Networks, Lipschitz Constrained Neural Networks, Chemical Processes, Model Predictive Control

*Corresponding author. E-mail: wuzhe@nus.edu.sg.

Please refer to <https://github.com/killingbear999/ICLRNN> for source codes.

1. Introduction

Neural networks provide a powerful tool to process modeling and control, an important engineering problem in various manufacturing industries such as chemical, pharmaceutical, and energy systems. This work draws inspiration from nature-inspired design to develop a fast and robust solution that addresses two crucial challenges: computational efficiency and robustness, for modeling and control of real-world nonlinear systems. Specifically, neural network models have been developed to capture complex nonlinear dynamics of industrial manufacturing systems, and the models can be further used for process monitoring, predictive maintenance, optimization, and real-time control. However, while neural network-based optimization can optimize process performance such as energy consumption and process profits, based on the prediction of neural networks, computational efficiency remains a big challenge for its real-time implementation. For example, model predictive control (MPC), an advanced optimization-based control technique, has been widely used to manage a process while complying with a set of constraints. Traditional MPC based on first-principles models encounters limitations, particularly in scenarios with intricate dynamics, where deriving these models proves infeasible. Over the past decades, neural network-based MPC (NN-MPC) has received increasing attention, where a neural network that models system dynamics is incorporated into the design of MPC optimization problems (Bao et al., 2017; Afram et al., 2017; Lanzetti et al., 2019; Ellis and Chinde, 2020; Nubert et al., 2020; Zheng et al., 2022a,b; Sitapure and Kwon, 2022). However, general optimization problems (e.g., MPC) built on conventional neural networks often fall short of meeting the requirement of computational efficiency. Nonetheless, efforts have been made to mitigate these limitations. For example, the computational efficiency of NN-MPC is enhanced by implementing an input convex architecture in neural networks (Wang et al., 2025). Additionally, robustness of NN-MPC is improved by developing Lipschitz-constrained neural networks (LNNs) (Tan and Wu, 2024).

In real-world applications, computational efficiency (for neural network-based optimization tasks) plays a pivotal role due to the imperative need for real-time decision-making, especially in critical engineering processes such as chemical process operations (Wang et al., 2025). We define computa-

tional efficiency as the speed at which computational tasks are completed within a given execution timeframe (in actual deployment to industrial engineering processes, the model is trained offline, and the costs associated with the training process are not a primary concern). An effective approach to achieving this efficiency is through the transformation from non-convex to convex structures. Convexity is a ubiquitous characteristic observed in various physical systems such as the potential energy function (Goldstein et al., 2002; Taylor and Taylor, 2005), magnetic fields (Purcell, 1963; Griffiths, 2005), and general relativity (Hartle, 2003).

Additionally, in real-world engineering applications, robustness plays a critical role due to the prevalent noise present in most real-world data, which significantly hampers neural network performance. Our definition of robustness aligns closely with the principles outlined by Tan and Wu (2024). Given the inherent noise in real-world process data, our goal is to improve neural networks by effectively learning from noisy training data for comprehensive end-to-end applications. Leveraging LNNs offers a potential solution to the robustness challenge. However, at this stage, the development of neural networks that address the above two challenges simultaneously remains an open question. It is important to note that the integration of input convexity and Lipschitz continuity in a single neural network presents a non-trivial challenge due to their interplay in the way that enforcing one property in the design of neural networks may compromise the other property.

Motivated by the above considerations, in this work, we introduce an Input Convex Lipschitz Recurrent Neural Network (ICLRNN) that amalgamates the strengths of input convexity and Lipschitz continuity. This approach aims to achieve the concurrent resolution of computational efficiency and robustness for real-world engineering applications. Specifically, we validate the efficacy of ICLRNN across various engineering problems that include neural network-based modeling and control for chemical processes and solar irradiance forecasting for energy systems. Performance assessment hinges on modeling accuracy, computational efficiency (i.e., evaluated by MPC runtime), model complexity (i.e., evaluated by the number of floating point operations (FLOPs)¹), and robustness

¹FLOPs, or floating-point operations, refer to the number of floating-point operations (such as addition, subtraction, multiplication, division, etc.) required to call the model once (i.e., a single forward pass through a model). It serves as a metric for evaluating and quantifying the complexity and computational demand of the model, where higher FLOPs indicate greater complexity.

against noise. Our objective is to achieve equilibrium across these dimensions as they hold equal importance in real-world engineering scenarios.

In summary, this work proposes an ICLRNN architecture, substantiating its theoretical attributes as input convex and Lipschitz continuous, and successfully implements and illustrates that ICLRNN surpasses state-of-the-art recurrent units in various engineering tasks, including modeling and control of chemical processes and real-time solar irradiance forecasting on real-world solar PV systems. The rest of this article is structured as follows: Section 2 introduces the class of systems and the design of neural network-based MPC. Section 3 provides an overview of the current family of recurrent units. Section 4 presents the proposed ICLRNN architecture and implementation, and proves that the architecture is both input convex and Lipschitz-constrained. Section 5 uses a chemical process example to validate the performance of ICLRNN in modeling and control ordinary differential equation (ODE) systems. Section 6 applies ICLRNN to solar irradiance forecasting on real-world solar PV systems.

2. Nonlinear Systems and Optimization

2.1. Notations

Let $L(f)$ represent the Lipschitz constant of a function f . “ \circ ” denotes composition. $\|\cdot\|$ and $\|\cdot\|_2$ denote spectral norm and Euclidean norm of a matrix, respectively. $\sigma(\cdot)$ denotes the singular value of a matrix.

2.1.1. Class of Systems

We consider a category of systems that can be expressed through the ordinary differential equations (ODEs) of the following form:

$$\dot{\mathbf{x}} = F(\mathbf{x}, \mathbf{u}) \tag{1}$$

where $\mathbf{u} \in \mathbb{R}^m$ denotes the control action and $\mathbf{x} \in \mathbb{R}^n$ denotes the state vector. The function $F : X \times U \rightarrow \mathbb{R}^n$ is continuously differentiable, where $X \subset \mathbb{R}^n$ and $U \subset \mathbb{R}^m$ are connected and compact subsets that enclose an open neighborhood around the origin respectively. In this context, we maintain the assumption throughout this task that $F(0,0) = 0$, ensuring that the origin $(\mathbf{x}, \mathbf{u}) = (0,0)$ serves as an equilibrium point. As it might be impractical to obtain first-

principles models for intricate real-world systems, our objective is to construct a neural network to model the nonlinear system specified by Eq. (1), embed it into optimization problems, and maintain computational efficiency and robustness simultaneously.

2.1.2. MPC Formulation

The optimization problem of the MPC that incorporates a ICLRNN as its predictive model is expressed as follows:

$$\mathcal{L} = \min_{\mathbf{u} \in S(\Delta)} \int_{t_k}^{t_{k+N}} J(\tilde{\mathbf{x}}(t), \mathbf{u}(t)) dt \quad (2a)$$

$$\text{s.t. } \dot{\tilde{\mathbf{x}}}(t) = F_{nn}(\tilde{\mathbf{x}}(t), \mathbf{u}(t)) \quad (2b)$$

$$\mathbf{u}(t) \in \mathbb{U}, \forall t \in [t_k, t_{k+N}) \quad (2c)$$

$$\tilde{\mathbf{x}}(t_k) = \mathbf{x}(t_k) \quad (2d)$$

where $S(\Delta)$ denotes the set of piecewise constant functions with period Δ , $\tilde{\mathbf{x}}$ denotes the predicted state trajectory, and N denotes the number of sampling periods in the prediction horizon. The objective function \mathcal{L} outlined in Eq. (2a) integrates a cost function J that depends on both the control actions \mathbf{u} and the system states \mathbf{x} . The system dynamic function $F_{nn}(\tilde{\mathbf{x}}(t), \mathbf{u}(t))$ expressed in Eq. (2b) is parameterized by an RNN (e.g., the proposed ICLRNN in this work). Eq. (2c) encapsulates the constraint function \mathbb{U} , delineating feasible control actions. Eq. (2d) establishes the initial condition $\tilde{\mathbf{x}}(t_k)$ in Eq. (2b), referring to the state measurement at $t = t_k$.

It is important to highlight that a convex neural network-based MPC remains convex even when making multi-step ahead predictions, where the prediction horizon is greater than one (Wang et al., 2025). This statement holds true if and only if the neural network embedded is inherently input convex and the neural network output is non-negative for certain objective functions (e.g., quadratic functions and absolute functions). In this case, MinMax scaling (i.e., transforming each feature by scaling it to a specified range, such as between 0 and 1, based on the training set) and the ReLU activation function in the final layer can be used to ensure non-negative outputs, thereby preserving the convexity of the optimization problem.

3. Family of Recurrent Units

We will first review related works, including recent advancements in high-performing recurrent units such as Input Convex RNNs and Lipschitz RNNs, among others.

3.0.1. Simple RNN

A simple RNN cell follows:

$$\mathbf{h}_t = g_1(\mathbf{W}^{(x)}\mathbf{x}_t + \mathbf{U}^{(h)}\mathbf{h}_{t-1} + \mathbf{b}^{(h)}) \quad (3a)$$

$$\mathbf{y}_t = g_2(\mathbf{W}^{(y)}\mathbf{h}_t + \mathbf{b}^{(y)}) \quad (3b)$$

where \mathbf{h}_t is the hidden state at time step t , \mathbf{x}_t is the input at time step t , \mathbf{h}_{t-1} is the hidden state from the previous time step, $\mathbf{W}^{(x)}$, $\mathbf{U}^{(h)}$ and $\mathbf{W}^{(y)}$ are weight matrices for the input, hidden state, and output respectively, $\mathbf{b}^{(h)}$ and $\mathbf{b}^{(y)}$ are the bias vectors for the hidden state and output respectively, and \mathbf{y}_t is the output at time step t .

3.1. High-performing RNNs

In recent years, several high-performing recurrent units have emerged, including UniCORNN (Rusch and Mishra, 2021), rank-coding based RNNs (Jeffares et al., 2021), and Linear Recurrent Units (Orvieto et al., 2023). However, these variants primarily emphasize enhancing accuracy, especially for very long time-dependent sequences modeling, often at the cost of model simplicity and computational efficiency. Moreover, in many engineering applications, accuracy alone does not dictate the suitability of a model. In fact, from an engineering point of view, simplicity and robustness are also important in addition to accuracy, as they ensure the model can be easily adapted and incorporated into existing industrial operational systems, and can be trusted in an uncertain environment with noise and disturbances. Therefore, the goal of this work is to develop a network architecture based on simple RNNs that strikes a balance between these factors while maintaining a satisfactory level of accuracy, rather than investigating the novel designs of RNNs for improved accuracy only.

3.2. Input Convex RNN

Building upon nature-inspired design and extending its application to neural networks, Input Convex Neural Networks (ICNNs) is a class of neural network architectures intentionally crafted to maintain convexity in their output with respect to the input. Leveraging these models could be particularly advantageous in various engineering problems, notably in applications such as MPC, due to their inherent benefits especially in optimization. This concept was first introduced as Feedforward Neural Networks (FNN) (Amos et al., 2017), and subsequently extended to Recurrent Neural Networks (RNN) (Chen et al., 2018), and Long Short-Term Memory (LSTM) (Wang et al., 2025).

The initiative behind ICNNs is to leverage the power of neural networks, specifically designed to maintain convexity within their decision boundaries (Amos et al., 2017). ICNNs aim to combine the strengths of neural networks in modeling complex data with the advantages of convex optimization, which ensures the convergence to a global optimal solution. They are particularly attractive for control and optimization problems, where achieving globally optimal solutions is essential. By maintaining convexity, ICNNs help ensure that the optimization problems associated with neural networks (e.g., neural network-based optimization) remain tractable, thus addressing some of the challenges of non-convexity and the potential for suboptimal local solutions in traditional neural networks. A foundational work, known as Input Convex RNN (ICRNN) (Chen et al., 2018), serves as one of the baselines. The output of ICRNN follows Chen et al. (2018):

$$\mathbf{h}_t = g_1(\mathbf{U}\hat{\mathbf{x}}_t + \mathbf{W}\mathbf{h}_{t-1} + \mathbf{D}_2\hat{\mathbf{x}}_{t-1}) \quad (4a)$$

$$\mathbf{y}_t = g_2(\mathbf{V}\mathbf{h}_t + \mathbf{D}_1\mathbf{h}_{t-1} + \mathbf{D}_3\hat{\mathbf{x}}_t) \quad (4b)$$

The output \mathbf{y}_t is convex with respect to the input $\hat{\mathbf{x}}_t$ if non-decreasing and convex activation functions are used for g_i , and $\{\mathbf{U}, \mathbf{W}, \mathbf{V}, \mathbf{D}_1, \mathbf{D}_2, \mathbf{D}_3\}$ are chosen to be non-negative weights, where $\hat{\mathbf{x}}_t$ denotes $[\mathbf{x}_t^\top, -\mathbf{x}_t^\top]^\top$.

3.3. Lipschitz RNN

By adhering to the definition of Lipschitz continuity for a function f , where an L -Lipschitz continuous f ensures that any minor perturbation to the input results in an output change of

at most L times the magnitude of that perturbation. Therefore, constraining neural networks to maintain Lipschitz continuity significantly fortifies their resilience against input perturbations. This concept was first introduced as FNN (Anil et al., 2019), and subsequently extended to RNN (Erichson et al., 2020), and Convolutional Neural Networks (CNN) (Serrurier et al., 2021). A pivotal work, namely the Lipschitz RNN (LRNN) (Erichson et al., 2020), stands as one of the baselines in this paper. The output of LRNN follows Erichson et al. (2020):

$$\dot{\mathbf{h}}_t = \mathbf{A}_{\beta_A, \gamma_A} \mathbf{h}_t + \tanh(\mathbf{W}_{\beta_W, \gamma_W} \mathbf{h}_t + \mathbf{U} \mathbf{x}_t + \mathbf{b}) \quad (5a)$$

$$\mathbf{y}_t = \mathbf{D} \mathbf{h}_t \quad (5b)$$

where $\beta_A, \beta_W \in [0, 1]$, $\gamma_A, \gamma_W > 0$ are tunable parameters, $\mathbf{M}_A, \mathbf{M}_W, \mathbf{D}, \mathbf{U}$ are trainable weights, $\dot{\mathbf{h}}$ is the time derivative of \mathbf{h} (i.e., \mathbf{h} can be updated by the explicit (forward) Euler scheme or a two-stage explicit Runge-Kutta scheme), and $\mathbf{A}_{\beta_A, \gamma_A}, \mathbf{W}_{\beta_W, \gamma_W}$ is computed as follows:

$$\mathbf{A}_{\beta_A, \gamma_A} = (1 - \beta_A)(\mathbf{M}_A + \mathbf{M}_A^T) + \beta_A(\mathbf{M}_A - \mathbf{M}_A^T) - \gamma_A \mathbf{I} \quad (6a)$$

$$\mathbf{W}_{\beta_W, \gamma_W} = (1 - \beta_W)(\mathbf{M}_W + \mathbf{M}_W^T) + \beta_W(\mathbf{M}_W - \mathbf{M}_W^T) - \gamma_W \mathbf{I} \quad (6b)$$

4. Input Convex Lipschitz Recurrent Neural Networks

In this section, we first introduce a novel Lipschitz-constrained, input convex network within the context of a simple RNN. We then provide theoretical proofs for both the Lipschitz continuity of the network, including an upper bound for its Lipschitz constant, and the input convexity, respectively.

4.1. Introduction to Input Convex Lipschitz RNN

We propose a novel Input Convex Lipschitz Recurrent Neural Networks, termed ICLRNN, that possesses both Lipschitz continuity and input convexity properties. Specifically, the output of ICLRNN is defined as follows:

$$\mathbf{h}_t = g_1(\mathbf{W}^{(x)} \mathbf{x}_t + \mathbf{U}^{(h)} \mathbf{h}_{t-1} + \mathbf{b}^{(h)}) \quad (7a)$$

$$\mathbf{y}_t = g_2(\mathbf{W}^{(y)} \mathbf{h}_t + \mathbf{b}^{(y)}) \quad (7b)$$

where $\{\mathbf{W}^{(x)}, \mathbf{W}^{(y)}, \mathbf{U}^{(x)}\}$ are constrained to be non-negative with largest singular values small and bounded by 1, and all g_i are constrained to be convex, non-decreasing, and Lipschitz continuous (e.g., ReLU). Similar to Chen et al. (2018), we **expand the input** as $\hat{\mathbf{x}}_t = [\mathbf{x}_t^\top, -\mathbf{x}_t^\top]^\top \in \mathbb{R}^{2n_x}$. Noted that the ICLRNN maintains the neural architecture of the simple RNN in Eq. (3) while introducing constraints on the weights and activation functions to ensure input convexity and Lipschitz continuity.

A neural network’s output inherits input convexity and Lipschitz continuity only if every hidden state possesses these properties. Unlike Chen et al. (2018) and Erichson et al. (2020), the ICLRNN enforces these properties by constraining the weights and activation functions rather than adding supplementary variables to the RNN architecture. This approach reduces network complexity and minimizes computational demands. Moreover, models such as LRNN, ICRNN, UniCORNN, and Linear Recurrent Units involve high FLOPs and lack theoretical guarantees on robustness and computational efficiency for neural network-based optimization problems. Many engineering applications can achieve satisfactory modeling accuracy with relatively simple neural network structures. However, improving the robustness and computational efficiency of these models for neural network-based optimization and control remains an important challenge. These considerations motivated the design choice to retain the standard RNN architecture while imposing input convexity and Lipschitz constraints on the weights.

4.2. Implementation of ICLRNN

First, we enforce the non-negative constraint in all weights by applying weight clipping, setting all negative weight values to zero, i.e.,

$$\mathbf{W} \leftarrow \max(\mathbf{W}, 0) \tag{8}$$

. Next, we perform spectral normalization on the non-negative weights, reducing the spectral norm of individual weights to at most 1, i.e.,

$$\mathbf{W} \leftarrow \frac{\mathbf{W}}{\sigma_{max}(\mathbf{W}) + \epsilon} \tag{9}$$

Algorithm 1: Power Iteration Method

Input: \mathbf{W} : the input matrix

Input: *maxiter*: maximum number of iterations

Input: *eps*: convergence tolerance (stopping criterion)

Output: σ_{max} : largest singular value (approximation)

Output: \mathbf{v} : corresponding singular vector (right singular vector)

1: Initialize a random vector \mathbf{v} of size n (e.g., $\mathbf{v} \sim Uniform(0, 1)$).

2: Normalize \mathbf{v} : $\mathbf{v} \leftarrow \frac{\mathbf{v}}{\|\mathbf{v}\|}$.

3: **for** *epoch* $\leftarrow 1, 2, \dots, maxiter$ **do**

4: Compute the matrix-vector product: $\mathbf{u} \leftarrow \mathbf{W}\mathbf{v}$.

5: Normalize \mathbf{u} : $\mathbf{u} \leftarrow \frac{\mathbf{u}}{\|\mathbf{u}\|}$.

6: Compute the next matrix-vector product: $\mathbf{v}_{new} \leftarrow \mathbf{W}^T \mathbf{u}$.

7: Normalize \mathbf{v}_{new} : $\mathbf{v}_{new} \leftarrow \frac{\mathbf{v}_{new}}{\|\mathbf{v}_{new}\|}$.

8: Check for convergence: if $\|\mathbf{v}_{new} - \mathbf{v}\| < eps$, break.

9: Update $\mathbf{v} \leftarrow \mathbf{v}_{new}$.

10: **end for**

11: Compute the largest singular value: $\sigma_{max} \leftarrow \|\mathbf{W}\mathbf{v}\|$.

12: Return σ_{max} and \mathbf{v} .

, where ϵ is a small constant to ensure that operator norm of normalized weight is strictly less than 1, e.g., 1×10^{-3} . To approximate $\sigma_{max}(\mathbf{W})$, we use the power iteration algorithm (see Algorithm 1), an iterative numerical method that computes the largest singular value by repeatedly multiplying the matrix by a vector and normalizing the result until convergence. The complete code is available in <https://github.com/killingbear999/ICLRNN>. While spectral normalization has been widely used to stabilize the training of generative adversarial networks (GANs) (Miyato et al., 2018), it is less commonly applied to RNNs.

Moreover, Serrurier et al. (2021) employs the Björck algorithm to ensure Lipschitz continuity by iteratively refining an initial estimate of an orthogonal matrix. This algorithm minimizes the error between the estimate and the true orthogonal matrix, gradually converging to a stable solution, and adjusts singular values to at most one. However, it is important to emphasize that the Björck algorithm should not be used in the ICLRNN. Unlike spectral normalization, which scales weights to ensure the spectral norm is bounded and inherently maintains non-negativity, the Björck algorithm introduces both positive and negative values during its orthogonalization process. This behavior is incompatible with the non-negativity constraint required in ICLRNN.

Additionally, regularization techniques such as dropout (Srivastava et al., 2014), batch normalization (Ioffe, 2015), and layer normalization (Ba, 2016) can help stabilize neural network training. However, these techniques introduce non-linear transformations, disrupting network convexity and thus should not be used in the training of ICNNs (e.g., the training of our ICLRNN).

At last, ICLRNN uses ReLU as the activation function for hidden states instead of the GroupSort function proposed in Anil et al. (2019). This decision aims to maintain convexity within the model architecture. Although GroupSort exhibits gradient norm preservation and higher expressive power (Tan and Wu, 2024), its non-convex nature contrasts with our primary objective.

Remark 1. *For ICNNs, including our proposed ICLRNN, we recommend applying MinMax scaling to the data prior to fitting it to the neural network. MinMax scaling is a normalization technique that transforms data to a specified range, usually between 0 and 1 (or another specified range). This technique **linearly** scales each feature x in the dataset \mathcal{X} individually based on its minimum and maximum values, i.e., $\forall x \in \mathcal{X}$:*

$$x \leftarrow \frac{x - \min(\mathcal{X})}{\max(\mathcal{X}) - \min(\mathcal{X})}(b - a) + a \quad (10)$$

where $\min(\mathcal{X})$ is the minimum value of the feature in the dataset, $\max(\mathcal{X})$ is the maximum value of the feature in the dataset, a is the lower bound of the desired range (default is 0), and b is the upper bound of the desired range (default is 1). This preprocessing step ensures that all feature values lie within the specified range, which can improve the stability and performance of the neural network.

4.3. Lipschitz Continuity of ICLRNN

We first list the definition of Lipschitz continuity and related lemmas for readers' reference, as follows:

Definition 1 ((Eriksson et al., 2013)). *A function $f : X \rightarrow \mathbb{R}$ is Lipschitz continuous with Lipschitz constant L (i.e., L -Lipschitz) if and only if the following inequality holds $\forall (x_1, x_2) \in X$:*

$$\|f(x_1) - f(x_2)\|_2 \leq L\|x_1 - x_2\|_2 \quad (11)$$

Definition 2. Given a linear function $f(\mathbf{x}) = \mathbf{W}\mathbf{x}$ with a weight $\mathbf{W} \in \mathbb{R}^{n \times m}$, we have:

$$L(f) = L(\mathbf{W}) = \|\mathbf{W}\| = \sigma_{\max}(\mathbf{W}) \quad (12)$$

Lemma 1. Consider a recurrence relation of the form, omitting the bias term:

$$\mathbf{h}_t = g(\mathbf{W}^{(x)}\mathbf{x}_t + \mathbf{U}^{(h)}\mathbf{h}_{t-1}) \quad (13)$$

where g represents a general transformation applied to the weighted inputs, $\mathbf{W}^{(x)}$ and $\mathbf{U}^{(h)}$ are weight matrices, and \mathbf{x}_t and \mathbf{h}_{t-1} are the inputs. The terms $\mathbf{W}^{(x)}\mathbf{x}_t$ and $\mathbf{U}^{(h)}\mathbf{h}_{t-1}$ contribute *independently* to the change in \mathbf{h}_t . The Lipschitz constant $L(\mathbf{h})$ of the mapping $\mathbf{x}_t, \mathbf{h}_{t-1} \rightarrow \mathbf{h}_t$ satisfies:

$$L(\mathbf{h}_t) \leq \max(L(\mathbf{W}^{(x)}), L(\mathbf{U}^{(h)})) \quad (14)$$

where $L(\mathbf{W}^{(x)})$ is the Lipschitz constant (or spectral norm) of the weight matrix $\mathbf{W}^{(x)}$ and $L(\mathbf{U}^{(h)})$ is the Lipschitz constant (or spectral norm) of the weight matrix $\mathbf{U}^{(h)}$.

Lemma 2 ((Eriksson et al., 2013)). Consider a set of functions, e.g., $f : X \rightarrow \mathbb{R}$ and $g : X \rightarrow \mathbb{R}$ with Lipschitz constants $L(f)$ and $L(g)$ respectively, by taking their composition, denoted as $h = f \circ g$, the Lipschitz constant $L(h)$ of the resultant function h satisfies:

$$L(h) \leq L(f) \times L(g) \quad (15)$$

Lemma 3 ((Virmaux and Scaman, 2018)). The most common activation functions such as ReLU, Sigmoid, and Tanh have a Lipschitz constant that equals 1, while Softmax has a Lipschitz constant bounded by 1.

Based on the previously stated lemmas, we present the following proposition regarding the upper bound for the Lipschitz constant of the ICLRNN.

Proposition 1. Consider the L -layer ICLRNN. The Lipschitz constant of the output \mathbf{y}_t is upper bounded by 1 if and only if all weights $\{\mathbf{W}^{(x)}, \mathbf{U}^{(h)}, \mathbf{W}^{(y)}\}$ and all activation functions g_i have a Lipschitz constant upper bounded by 1.

Proof. By unrolling the recurrent operations over time t in Eq. (7), the output of ICLRNN can be described as a function, omitting the bias term:

$$\mathbf{y}_t = g_t^{(y)}(\mathbf{W}^{(y)} g_t^{(h)}(\mathbf{W}^{(x)} \mathbf{x}_t + \mathbf{U}^{(h)} g_{t-1}^{(h)}(\mathbf{W}^{(x)} \mathbf{x}_{t-1} + \mathbf{U}^{(h)} \dots g_1^{(h)}(\mathbf{W}^{(x)} \mathbf{x}_1 + \mathbf{U}^{(h)} \mathbf{h}_0))) \quad (16)$$

Thus, the Lipschitz constant of an ICLRNN is upper bounded by the product of the individual Lipschitz constants (i.e., Lemma 1 and Lemma 2):

$$L(\mathbf{y}_t) \leq L(g_t^{(y)}) \times L(\mathbf{W}^{(y)}) \times L(g_t^{(h)}) \times \max(L(\mathbf{W}^{(x)}), L(\mathbf{U}^{(h)})) \times \dots \times L(g_1^{(h)}) \times \max(L(\mathbf{W}^{(x)}), L(\mathbf{U}^{(h)})) \quad (17)$$

By ensuring that the Lipschitz constants of all weights $\{\mathbf{W}^{(x)}, \mathbf{U}^{(h)}, \mathbf{W}^{(y)}\}$ in the ICLRNN are upper bounded by 1 through spectral normalization, and that all activation functions g_i , such as ReLU, have Lipschitz constants also bounded by 1, the Lipschitz constant of the final output of the ICLRNN is guaranteed to be upper bounded by 1. \square

Remark 2. *Since the function approximated by RNNs is not analytically tractable, we estimate the Lipschitz constant L of the neural network numerically, as follows:*

$$L \approx \max_{x, y \in \mathbb{D}} \frac{\|f(x) - f(y)\|}{\|x - y\|} \quad (18)$$

where \mathbb{D} is the domain of interest. To approximate L , we generate random pairs of $x, y \in \mathbb{D}$ and compute the ratio for each pair, increasing the sampling density to enhance the accuracy of the estimate. For more accurate techniques to estimate the Lipschitz constant of deep neural networks, interested readers are encouraged to refer to Virmaux and Scaman (2018); Fazlyab et al. (2019); Latorre et al. (2020).

4.4. Input Convexity of ICLRNN

Similarly, we present the definition of convexity for readers' reference, as follows:

Definition 3 ((Boyd and Vandenberghe, 2004)). *A function $f : X \rightarrow \mathbb{R}$ is convex if and only if the following inequality holds $\forall (x_1, x_2) \in X$, with $x_1 \neq x_2$, and $\forall \lambda \in (0, 1)$:*

$$f(\lambda x_1 + (1 - \lambda)x_2) \leq \lambda f(x_1) + (1 - \lambda)f(x_2) \quad (19)$$

and it is strictly convex if the relation \leq becomes $<$.

Next, we develop the following proposition to show the convexity of L -layer ICLRNN.

Proposition 2. *Consider the L -layer ICLRNN. The output \mathbf{y}_t is input convex if and only if all weights $\{\mathbf{W}^{(x)}, \mathbf{U}^{(h)}, \mathbf{W}^{(y)}\}$ are non-negative and all activation functions g_i are convex and non-decreasing.*

Proof. With Eq. (16), the proof directly follows from the fact that affine transformations with non-negative matrices and compositions of convex non-decreasing functions preserve convexity (Boyd and Vandenberghe, 2004). \square

With Propositions 1 and 2, we present the following theorem to demonstrate that the ICLRNN is both input convex and Lipschitz-constrained.

Theorem 1. *Consider the L -layer ICLRNN. Each element of the output \mathbf{y}_t is a convex, non-decreasing function of the input $\hat{\mathbf{x}}_t = [\mathbf{x}_t^\top, -\mathbf{x}_t^\top]^\top$ (or just \mathbf{x}_t), with the Lipschitz constant upper bounded by 1, at each time step $t = 1, 2, \dots, t$, for all $\hat{\mathbf{x}}_t \in D \times D$ in a convex feasible space, provided that the following conditions are met: (1) All weights are non-negative, and their largest singular value is at most 1 at each time step t ; (2) All activation functions are convex, non-decreasing, and Lipschitz continuous (e.g., ReLU) at each time step t .*

Proof. Using Proposition 1 and Proposition 2, we can demonstrate that the Lipschitz constant of the ICLRNN is upper-bounded by 1 and that it is input-convex. The Lipschitz constant is bounded by 1 because the weight matrices are spectral-normalized. Furthermore, since the weights are non-negative and the activation functions are convex and non-decreasing, the overall function remains convex. The proof follows directly from the fact that spectral normalization preserves convexity, as it is a linear transformation. Therefore, the ICLRNN is both input-convex and Lipschitz-constrained. \square

5. Modeling and Control on a Chemical Process

In this section, we showcase the performance of the ICLRNN in modeling an ODE system through an example of a continuous stirred tank reactor (CSTR).

5.1. CSTR Modeling

This reaction facilitates the conversion of reactant A into product B . The CSTR incorporates a heating jacket responsible for supplying or extracting heat at a rate Q . The dynamic model of the CSTR is characterized by the ensuing material and energy balance equations:

$$\frac{dC_A}{dt} = \frac{F}{V}(C_{A0} - C_A) - k_0 e^{\frac{-E}{RT}} C_A^2 \quad (20a)$$

$$\frac{dT}{dt} = \frac{F}{V_L}(T_0 - T) + \frac{-\Delta H}{\rho_L C_p} k_0 e^{\frac{-E}{RT}} C_A^2 + \frac{Q}{\rho_L C_p V} \quad (20b)$$

where C_A denotes the concentration of reactant A , F denotes the volumetric flow rate, V_L denotes the volume of the reactant, C_{A0} denotes the inlet concentration of reactant A , k_0 denotes the pre-exponential constant, E denotes the activation energy, R denotes the ideal gas constant, T denotes the temperature, T_0 denotes the inlet temperature, ΔH denotes the enthalpy of reaction, ρ_L denotes the constant density of the reactant, C_p denotes the heat capacity, and Q denotes the heat input rate. Moreover, $\mathbf{x}^T = [C_A - C_{As}, T - T_s]$ denotes the system states, where $T - T_s$ and $C_A - C_{As}$ represent the deviations in the temperature of the reactor and the concentration of A from their respective steady-state values. $\mathbf{u}^T = [\Delta C_{A0}, \Delta Q]$ denotes the control actions, where $\Delta Q = Q - Q_s$ and $\Delta C_{A0} = C_{A0} - C_{A0s}$ denote the manipulated inputs within this system, representing the alterations in the heat input rate and the inlet concentration of reactant A , respectively. In summary, the inputs consist of $[T_t - T_s, C_{A,t} - C_{As}, \Delta Q_t, \Delta C_{A0,t}]$ at the current time step t . The outputs entail the state trajectory $[T_{t+1:n} - T_s, C_{A,t+1:n} - C_{As}]$ over the subsequent n time steps. In this case, n is set to 10. We conduct open-loop simulations for the CSTR of Eq. (20) using explicit Euler method. These simulations aim to collect data that mimics the real-world data for neural network training purposes. The detailed parameter values are listed in Table 1.

5.2. Modeling Performance

To evaluate the model’s robustness against noise, we introduce Gaussian noise to the training data (i.e., output trajectory \mathbf{y}), in an additive manner² as follows:

$$\mathbf{y}_i \leftarrow \mathbf{y}_i + z_i \quad (21)$$

where z_i is independently and identically distributed, drawn from a zero-mean normal distribution with variance N (the degree of noise), i.e., $z \sim \mathcal{N}(0, N)$. All models undergo training and evaluation using uniform configurations, incorporating a MinMax Scaling (i.e., scaling the data into a specific range between 0 and 1), a batch size of 256, a two-layer neural architecture with 64 neurons per layer (i.e., model size of (64, 64)), the mean-squared error (MSE) loss function, and the Adam optimizer. Detailed hyperparameter values, including the FLOPs to quantify model complexity, are listed in Table 2.

In Fig. 1, the left plot shows the mean testing MSE versus the degree of additive noise over three random trials in a linear scale, while the right plot presents the mean and standard deviation of the testing MSE versus the degree of additive noise over three random trials in a logarithmic scale for better clarity. Similarly, in Fig. 2, the left plot illustrates the mean Lipschitz constant of the trained model versus the degree of additive noise over three random trials in a linear scale, and the right plot displays the mean and standard deviation of the Lipschitz constant versus the degree of additive noise in a logarithmic scale for improved visualization. The Lipschitz constant of the trained model is estimated using numerical methods (see Remark 2). The solid line represents the mean across three trials on different unseen reactions, while the shaded region indicates the standard deviation.

From Figs. 1 and 2, it is evident that conventional recurrent units, such as standard RNN and LSTM, lack robustness against noise. The higher Lipschitz constant observed for LSTM compared to RNN under increasing noise levels may result from overfitting to noisy data, likely due to its

²Additive noise is more common in general applications like machine learning, sensor data, and most engineering fields because it aligns with the assumption of independent, Gaussian noise, while relative noise is more specific to cases where the noise source is tied to the signal’s magnitude, such as in financial systems, biology, and some physics domains.

advanced gating mechanisms. In contrast, LRNN, ICRNN, and ICLRNN demonstrate robustness across different noise levels, maintaining small Lipschitz constants (less than 1), meaning they exhibit 1-Lipschitz behavior across various noise levels. Although ICRNN does not theoretically satisfy the Lipschitz property, the convexity constraint effectively enhances its robustness to noise. This robustness likely arises because the convexity constraint simplifies the model’s learning capability, enabling it to learn non-convex functions (such as noisy data) through convex approximations. This simplification inherently helps prevent “overfitting” to noise during training.

The advantage of ICLRNN over LRNN lies in its lower testing MSE, indicating higher accuracy in modeling the system (see Fig. 1), and its significantly lower FLOPs, reflecting reduced model complexity. Specifically, for a 2-layer architecture with 64 neurons per layer, LRNN requires 159,508 FLOPs, whereas ICLRNN only requires 28,436 FLOPs - approximately 5.6 times fewer (see Table 2). This demonstrates that a less complex model can achieve more accurate results.

Similarly, ICLRNN offers a significant advantage over ICRNN in terms of FLOPs, representing a less complex model under the same neural architecture. For a 2-layer architecture with 64 neurons per layer, ICRNN requires 79,892 FLOPs, while ICLRNN only requires 28,436 FLOPs - approximately 2.8 times fewer (see Table 2). Additionally, ICRNN has a theoretical structural limitation in that its hypothesis space cannot be very large. Due to the introduction of additional trainable parameters in the standard RNN architecture, ICRNN performs well when the hypothesis space is small (e.g., 2 layers with less than 128 neurons per layer). However, as the hypothesis space increases (e.g., 2 layers with more than 128 neurons per layer), training becomes unstable (see Table 3). This instability results in the MSE becoming Not a Number (NaN)³, rendering the model untrainable unless stabilization techniques like layer normalization or batch normalization are employed. However, such techniques should be avoided in ICNN training because they introduce nonlinear scaling, violating the input convexity property of the final model. In summary, as the hypothesis space grows (e.g., by increasing the number of neurons), ICRNN’s testing MSE rises and

³In computing, NaN, which stands for “Not a Number”, is a numeric data type that represents an undefined or unrepresentable value. It can be used to represent: infinity, the result of dividing by zero, a missing value, and the square root of a negative number.

eventually becomes NaN, whereas ICLRNN maintains a small and stable testing MSE.

5.3. MPC Performance

Next, incorporating an ICNN (e.g., ICLRNN) into the aforementioned MPC in Eq. (2) transforms it into a convex optimization problem. Subsequently, PyIpopt, as a Python version of IPOPT (Wächter and Biegler, 2006), is used to address the MPC problem. The integration time step is set at $h_c = 1 \times 10^{-4}$ hr, while the sampling period remains $\Delta = 5 \times 10^{-3}$ hr. Additionally, we introduce a Lyapunov constraint to the system, as follows:

$$V(\tilde{\mathbf{x}}(t)) < V(\mathbf{x}(t_k)), \forall t \in [t_k, t_{k+N}) \quad (22)$$

where the Lyapunov-based constraint V is used to ensure closed-loop stability within MPC by mandating a decrease in the value of $V(x)$ ⁴. The design of the Lyapunov function, denoted as $V(\mathbf{x}) = \mathbf{x}^\top \mathbf{P} \mathbf{x}$, involves configuring the positive definite matrix \mathbf{P} as $\begin{bmatrix} 1060 & 22 \\ 22 & 0.52 \end{bmatrix}$, which ensures the convexity of the MPC.

We execute MPC for a fixed timeframe on an Intel Core i7-12700 processor with 64 GB of RAM for various models and repeat with various initial conditions to evaluate the performance of different NN-based MPC. Fig. 3 shows one of the initial conditions, from which it is evident that the ICLRNN-based MPC converges, whereas other NN-based MPC models do not. The fastest convergence speed highlights the superior computational efficiency of the ICLRNN-based MPC.

Moreover, it is important to highlight that ICLRNN-based MPC consistently demonstrates the fastest convergence speed across various initial conditions, thereby surpassing the state-of-the-art methodologies. Figs. 4 and 5 provide compelling evidence that the ICLRNN-based MPC achieves convergence, unlike other NN-based MPC, within a fixed timeframe. This outcome distinctly indicates that ICLRNN-based MPC exhibits the fastest convergence speed under identical settings.

In Fig. 4, the left panels show the results corresponding to the initial condition set at $[-1.5 \text{ kmol/m}^3, 70 \text{ K}]$. Specifically, the top left panel displays the concentration profile, the middle left panel shows the temperature, and the bottom left panel exhibits the converging path. Additionally,

⁴Lyapunov functions $V(x)$ are analogous to energy functions in some sense that the system is stable at the lowest energy point where $V(x) = 0$ at $x = 0$.

the right panels showcase the results from the initial condition at $[1.5 \text{ kmol}/\text{m}^3, -70 \text{ K}]$, featuring the concentration profile in the top right panel, temperature profile in the middle right panel, and the converging path in the bottom right panel. Moving to Fig. 5, the left panels depict the results obtained from the initial condition of $[-1.25 \text{ kmol}/\text{m}^3, 50 \text{ K}]$. Here, the top left panel represents the concentration, the middle left panel illustrates the temperature, and the bottom left panel shows the converging path. Similarly, the right panels exhibit the results of the initial condition at $[1.25 \text{ kmol}/\text{m}^3, -50 \text{ K}]$. In summary, across various initial conditions, ICLRNN-based MPC consistently demonstrates the fastest convergence speed, thereby surpassing the state-of-the-art methods.

6. Application to Real-World Solar Irradiance Prediction

In this section, we aim to forecast solar irradiance using real-time data for LHT Holdings, a wood pallet manufacturing industry based in Singapore.

6.1. System Description and Modeling

Before the installation of the solar photovoltaic (PV) system, LHT Holdings relied solely on the main utility grid to fulfill its energy needs. The solar PV system was successfully installed by 10 Degree Solar in late 2022 (the manufacturing pipeline of LHT Holdings and the solar PV system is described in our previous work (Wang et al., 2025)). This transition to solar energy was primarily driven by the aim of minimizing manufacturing costs. Three significant uncertainties were identified within the industry, namely solar irradiance affecting the solar PV system’s efficiency, the dynamic real-time pricing of energy sourced from the main utility grid, and the fluctuating energy demand stemming from unexpected customer orders.

Currently, the industrial facility relies primarily on solar PV as its main energy source, with the main utility grid serving as a backup. Excess solar energy is stored for later use. Accurate solar irradiance forecasting is crucial for efficient energy planning and cost reduction. Using sensors installed by the Solar Energy Research Institute of Singapore (SERIS) and Singapore Institute of Manufacturing Technology (SIMTech), including irradiance, humidity, wind, and temperature sensors, data is systematically recorded on a minute-by-minute basis and seamlessly uploaded online

into the system. Alongside data similar to that used by Zelikman et al. (2020), we predict minute-by-minute solar irradiance to optimize energy dispatch. In this time-series forecasting task, all models undergo training and evaluation using identical settings. These settings encompass model size of (256, 256), MSE as the loss function, and the Adam Optimizer. For the training and validation phases, we use data spanning from January 14, 2023, to December 16, 2023. Subsequently, data from December 17, 2023, to January 1, 2024, is exclusively reserved for testing and evaluating the models’ predictive performance.

Furthermore, from an engineering perspective, the training and implementation of neural network models are often constrained by limited computational resources, which are typically not as ample as those in computer science. Consequently, engineering applications require relatively simple models capable of effectively handling challenges such as data noise and convexity. To ensure the selection of the most suitable model, it is essential to conduct comparisons under consistent settings (i.e., the same model complexity). This approach ensures fairness, as we evaluate not only accuracy, but also other critical factors such as model complexity, which can be quantified by FLOPs.

6.2. Performance Analysis for Solar Irradiance Forecasting

We leverage FLOPs as a measure to assess the model complexity. As depicted in Table 4, it is evident that among all the models, ICLRNN demonstrates the most efficient computational performance as a result of its lowest FLOPs (excluding plain RNN). Consequently, this superior efficiency positions ICLRNN as the top-performing model when considering computational resources.

Given the real-world context of this task, introducing artificial noise for evaluating non-adversarial robustness becomes unnecessary as the inherent noise within real-world data suffices. Notably, our observations reveal that ICRNN encounters challenges with training when the hypothesis space size is large (i.e., the number of hidden neurons per layer is more than 128), thereby hindering its ability to effectively model complex system dynamics. While RNN and LSTM exhibit a limited capacity to capture system dynamics, they struggle notably when faced with sudden changes in solar irradiance, leading to less accurate predictions.

In Fig. 6a, we present results from the best state-of-the-art model, LRNN, alongside our model’s outcomes specifically for December 28, 2023. The LRNN, constrained by Lipschitz continuity, ex-

hibits significantly improved performance compared to the RNN and LSTM models. However, it still encounters challenges in accurately predicting solar irradiance during sudden fluctuations, and its excessively high FLOPs signify its computational intensity (i.e., 2,498,562 for LRNN compared to 401,410 for ICLRNN). Moreover, slight fluctuations in the LRNN predictions occur during periods of minimal solar irradiance at the start and end of the day. Highlighted within Fig. 6b, our ICLRNN outperforms LRNN and other state-of-the-art models, particularly in accurately predicting sudden changes in solar irradiance, which highlights the superior predictive capability of ICLRNN, showcasing its effectiveness in capturing and predicting nuanced fluctuations within the solar irradiance data. Notably, these observations persist across all trials and are not specific solely to December 28, 2023.

Specifically, Fig. 7 shows the model performance on solar irradiance prediction on December 28, 2023. The top two figures display the RNN and LSTM prediction outcomes, respectively. Both models demonstrate poor performance, failing to adjust adequately when faced with sudden changes in solar irradiance, leading to overshooting. Moreover, the middle two figures reveal that the ICRNN encounters issues related to the exploding gradient problem, particularly when the hypothesis space size becomes excessively large. The middle left figure shows the prediction performance of ICRNN with 128 hidden neurons per layer, while the middle right figure shows the prediction performance of ICRNN with 256 hidden neurons per layer. When surpassing 128 hidden neurons per layer, the ICRNN struggles to effectively capture and learn the system’s dynamics. Notably, these observations persist across all trials and are not specific solely to December 28, 2023. It is clearly shown in Fig. 7 that our ICLRNN model surpasses state-of-the-art models, demonstrating superior predictive capabilities across various scenarios.

7. Conclusion

This work introduces an Input Convex Lipschitz RNN to improve computational efficiency and robustness of neural networks in various engineering applications such as real-world solar irradiance prediction, and process modeling and control. The ICLRNN model was demonstrated to surpass state-of-the-art recurrent units across various engineering tasks, ranging from simulated studies to

real-world applications, in both computational efficiency and robustness.

8. Acknowledgments

Financial support from the A*STAR MTC YIRG 2022 Grant (222K3024) and NRF-CRP Grant 27-2021-0001 is gratefully acknowledged.

References

- Afram, A., Janabi-Sharifi, F., Fung, A.S., Raahemifar, K., 2017. Artificial Neural Network (ANN) Based Model Predictive Control (MPC) and Optimization of HVAC Systems: A State of the Art Review and Case Study of a Residential HVAC System. *Energy and Buildings* 141, 96–113.
- Amos, B., Xu, L., Kolter, J.Z., 2017. Input Convex Neural Networks, in: *International Conference on Machine Learning*, PMLR. pp. 146–155.
- Anil, C., Lucas, J., Grosse, R., 2019. Sorting out Lipschitz Function Approximation, in: *International Conference on Machine Learning*, PMLR. pp. 291–301.
- Ba, J.L., 2016. Layer Normalization. *arXiv preprint arXiv:1607.06450* .
- Bao, X., Sun, Z., Sharma, N., 2017. A Recurrent Neural Network Based MPC for a Hybrid Neuroprosthesis System, in: *2017 IEEE 56th Annual Conference on Decision and Control (CDC)*, IEEE. pp. 4715–4720.
- Boyd, S.P., Vandenberghe, L., 2004. *Convex Optimization*. Cambridge University Press.
- Chen, Y., Shi, Y., Zhang, B., 2018. Optimal Control via Neural Networks: A Convex Approach. *arXiv preprint arXiv:1805.11835* .
- Ellis, M.J., Chinde, V., 2020. An Encoder-Decoder LSTM-Based EMPC Framework Applied to a Building HVAC System. *Chemical Engineering Research and Design* 160, 508–520.
- Erichson, N.B., Azencot, O., Queiruga, A., Hodgkinson, L., Mahoney, M.W., 2020. Lipschitz Recurrent Neural Networks. *arXiv preprint arXiv:2006.12070* .
- Eriksson, K., Estep, D., Johnson, C., 2013. *Applied Mathematics: Body and Soul: Volume 1: Derivatives and Geometry in IR3*. Springer Science & Business Media.
- Fazlyab, M., Robey, A., Hassani, H., Morari, M., Pappas, G., 2019. Efficient and Accurate Estimation of Lipschitz Constants for Deep Neural Networks. *Advances in neural information processing systems* 32.

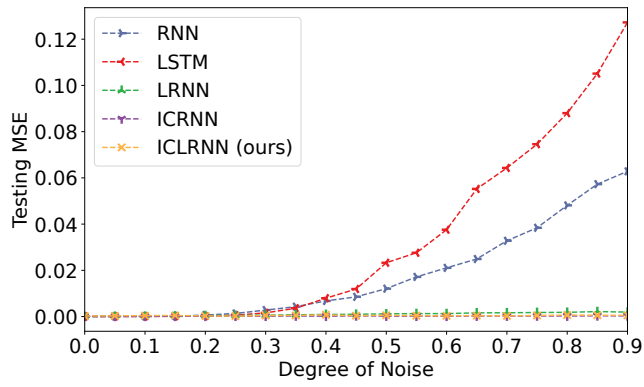
- Goldstein, H., Poole, C., Safko, J., 2002. Classical Mechanics.
- Griffiths, D.J., 2005. Introduction to Electrodynamics.
- Hartle, J.B., 2003. Gravity: an Introduction to Einstein’s General Relativity.
- Ioffe, S., 2015. Batch Normalization: Accelerating Deep Network Training by Reducing Internal Covariate Shift. arXiv preprint arXiv:1502.03167 .
- Jeffares, A., Guo, Q., Stenetorp, P., Moraitis, T., 2021. Spike-Inspired Rank Coding for Fast and Accurate Recurrent Neural Networks. arXiv preprint arXiv:2110.02865 .
- Lanzetti, N., Lian, Y.Z., Cortinovis, A., Dominguez, L., Mercangöz, M., Jones, C., 2019. Recurrent Neural Network Based MPC for Process Industries, in: 2019 18th European Control Conference (ECC), IEEE. pp. 1005–1010.
- Latorre, F., Rolland, P., Cevher, V., 2020. Lipschitz Constant Estimation of Neural Networks via Sparse Polynomial Optimization. arXiv preprint arXiv:2004.08688 .
- Miyato, T., Kataoka, T., Koyama, M., Yoshida, Y., 2018. Spectral Normalization for Generative Adversarial Networks. arXiv preprint arXiv:1802.05957 .
- Nubert, J., Köhler, J., Berenz, V., Allgöwer, F., Trimpe, S., 2020. Safe and Fast Tracking on a Robot Manipulator: Robust MPC and Neural Network Control. IEEE Robotics and Automation Letters 5, 3050–3057.
- Orvieto, A., Smith, S.L., Gu, A., Fernando, A., Gulcehre, C., Pascanu, R., De, S., 2023. Resurrecting Recurrent Neural Networks for Long Sequences, in: International Conference on Machine Learning, PMLR. pp. 26670–26698.
- Purcell, E.M., 1963. Electricity and Magnetism. Berkeley University 2.
- Rusch, T.K., Mishra, S., 2021. Unicornn: A Recurrent Model for Learning very Long Time Dependencies, in: International Conference on Machine Learning, PMLR. pp. 9168–9178.

- Serrurier, M., Mamalet, F., González-Sanz, A., Boissin, T., Loubes, J.M., Del Barrio, E., 2021. Achieving Robustness in Classification using Optimal Transport with Hinge Regularization, in: Proceedings of the IEEE/CVF Conference on Computer Vision and Pattern Recognition, pp. 505–514.
- Sitapure, N., Kwon, J.S.I., 2022. Neural Network-Based Model Predictive Control for Thin-film Chemical Deposition of Quantum Dots using Data from a Multiscale Simulation. *Chemical Engineering Research and Design* 183, 595–607.
- Srivastava, N., Hinton, G., Krizhevsky, A., Sutskever, I., Salakhutdinov, R., 2014. Dropout: A Simple Way to Prevent Neural Networks from Overfitting. *The journal of machine learning research* 15, 1929–1958.
- Tan, W.G.Y., Wu, Z., 2024. Robust Machine Learning Modeling for Predictive Control using Lipschitz-Constrained Neural Networks. *Computers & Chemical Engineering* 180, 108466.
- Taylor, J.R., Taylor, J.R., 2005. *Classical Mechanics*. volume 1. Springer.
- Virmaux, A., Scaman, K., 2018. Lipschitz Regularity of Deep Neural Networks: Analysis and Efficient Estimation. *Advances in Neural Information Processing Systems* 31.
- Wächter, A., Biegler, L.T., 2006. On the Implementation of an Interior-Point FilterLine-Search Algorithm for Large-Scale Nonlinear Programming. *Mathematical programming* 106, 25–57.
- Wang, Z., Yu, D., Wu, Z., 2025. Real-Time Machine-Learning-Based Optimization Using Input Convex Long Short-Term Memory Network. *Applied Energy* 377, 124472.
- Zelikman, E., Zhou, S., Irvin, J., Raterink, C., Sheng, H., Avati, A., Kelly, J., Rajagopal, R., Ng, A.Y., Gagne, D., 2020. Short-Term Solar Irradiance Forecasting using Calibrated Probabilistic Models. arXiv preprint arXiv:2010.04715 .
- Zheng, Y., Wang, X., Wu, Z., 2022a. Machine Learning Modeling and Predictive Control of the Batch Crystallization Process. *Industrial & Engineering Chemistry Research* 61, 5578–5592.

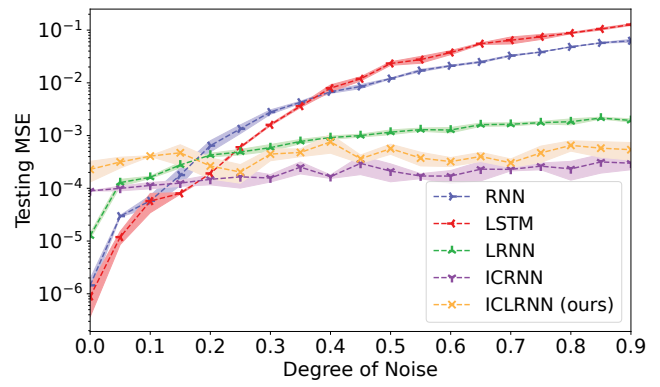
Zheng, Y., Zhao, T., Wang, X., Wu, Z., 2022b. Online Learning-Based Predictive Control of Crystallization Processes under Batch-to-Batch Parametric Drift. *AIChE Journal* 68, e17815.

List of Figures

1	Mean testing MSE vs. degree of additive noise over 3 random trials.	28
2	Mean Lipschitz constant of the trained model vs. degree of additive noise over 3 random trials.	29
3	MPC converging path in a fixed timeframe with an initial condition at $[-1.5 \text{ kmol}/\text{m}^3, 70 \text{ K}]$	30
4	Concentration profile (top left), temperature profile (middle left), converging path (bottom left) in a fixed timeframe with an initial condition at $[-1.5 \text{ kmol}/\text{m}^3, 70 \text{ K}]$ under MPC, and concentration profile (top right), temperature profile (middle right), converging path (bottom right) in a fixed timeframe with an initial condition at $[1.5 \text{ kmol}/\text{m}^3, -70 \text{ K}]$	31
5	Concentration profile (top left), temperature profile (middle left), converging path (bottom left) in a fixed timeframe with an initial condition at $[-1.25 \text{ kmol}/\text{m}^3, 50 \text{ K}]$, and concentration profile (top right), temperature profile (middle right), converging path (bottom right) in a fixed timeframe with an initial condition at $[1.25 \text{ kmol}/\text{m}^3, -50 \text{ K}]$	32
6	Solar irradiance forecasting performance of LRNN and ICLRNN on 2023-12-28.	33
7	RNN (top left), LSTM (top right), ICRNN (middle left and middle right with neural architecture of (128, 128) and (256, 256) respectively), LRNN (bottom left), and ICLRNN (bottom right) performance on 2023-12-28 for solar irradiance prediction.	34



(a) Linear scale



(b) Logarithmic scale

Figure 1: Mean testing MSE vs. degree of additive noise over 3 random trials.

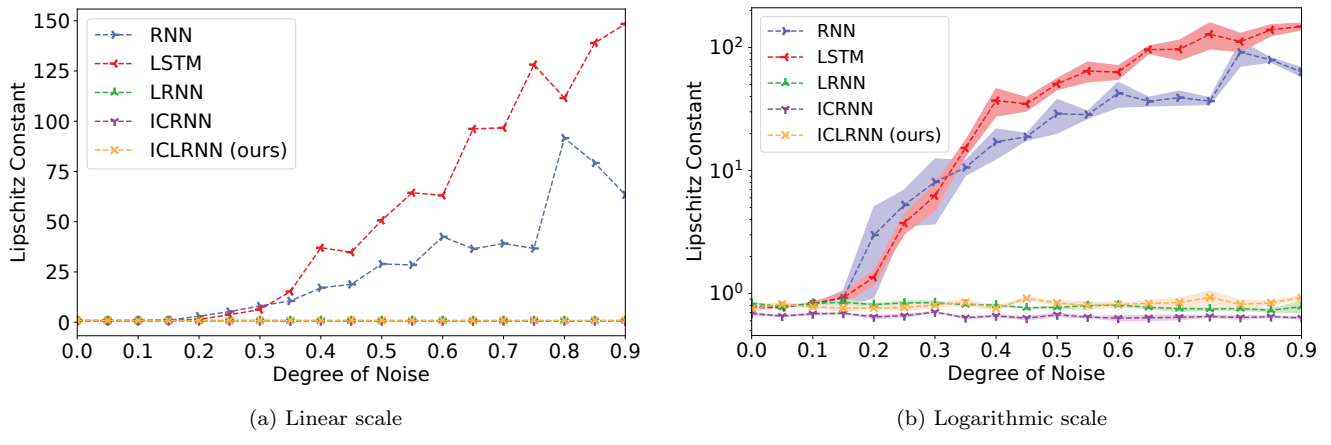


Figure 2: Mean Lipschitz constant of the trained model vs. degree of additive noise over 3 random trials.

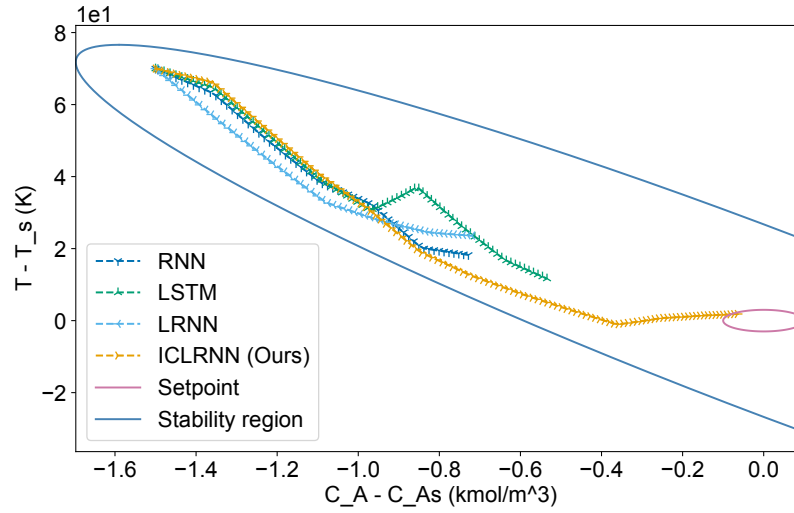


Figure 3: MPC converging path in a fixed timeframe with an initial condition at $[-1.5 \text{ kmol/m}^3, 70 \text{ K}]$.

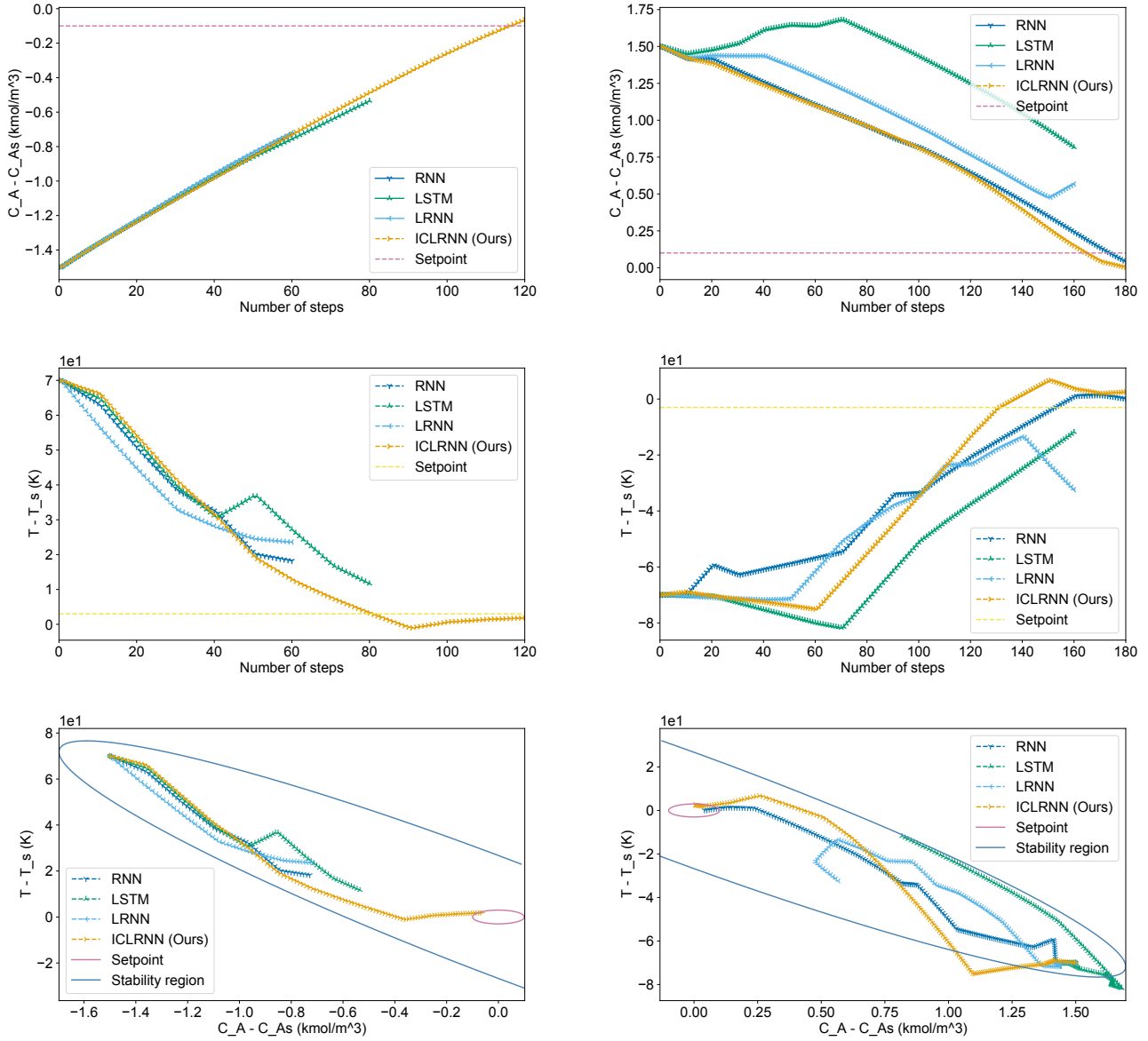


Figure 4: Concentration profile (top left), temperature profile (middle left), converging path (bottom left) in a fixed timeframe with an initial condition at $[-1.5 \text{ kmol/m}^3, 70 \text{ K}]$ under MPC, and concentration profile (top right), temperature profile (middle right), converging path (bottom right) in a fixed timeframe with an initial condition at $[1.5 \text{ kmol/m}^3, -70 \text{ K}]$.

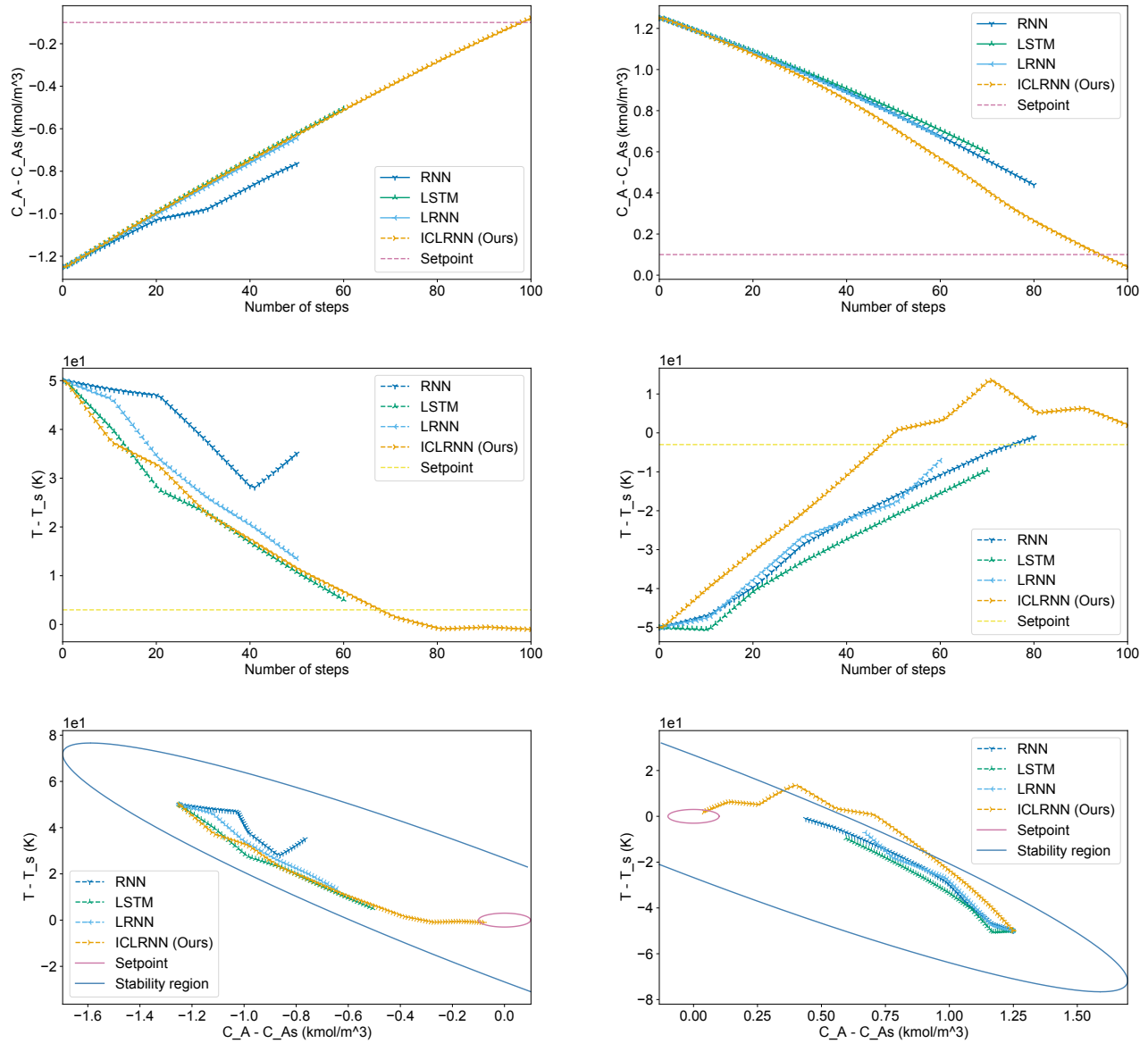
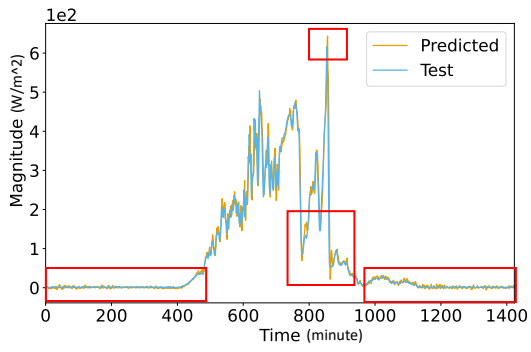
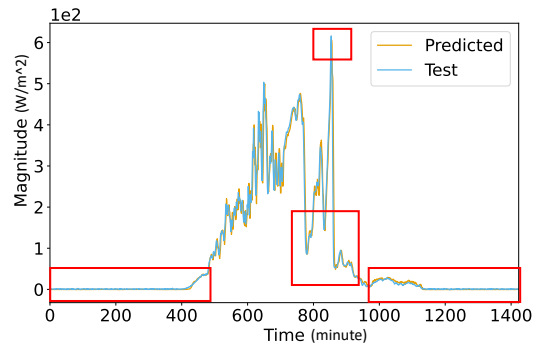


Figure 5: Concentration profile (top left), temperature profile (middle left), converging path (bottom left) in a fixed timeframe with an initial condition at $[-1.25 \text{ kmol/m}^3, 50 \text{ K}]$, and concentration profile (top right), temperature profile (middle right), converging path (bottom right) in a fixed timeframe with an initial condition at $[1.25 \text{ kmol/m}^3, -50 \text{ K}]$.



(a) LRNN performances on 2023-12-28 for solar irradiance prediction.



(b) ICLRNN performances on 2023-12-28 for solar irradiance prediction.

Figure 6: Solar irradiance forecasting performance of LRNN and ICLRNN on 2023-12-28.

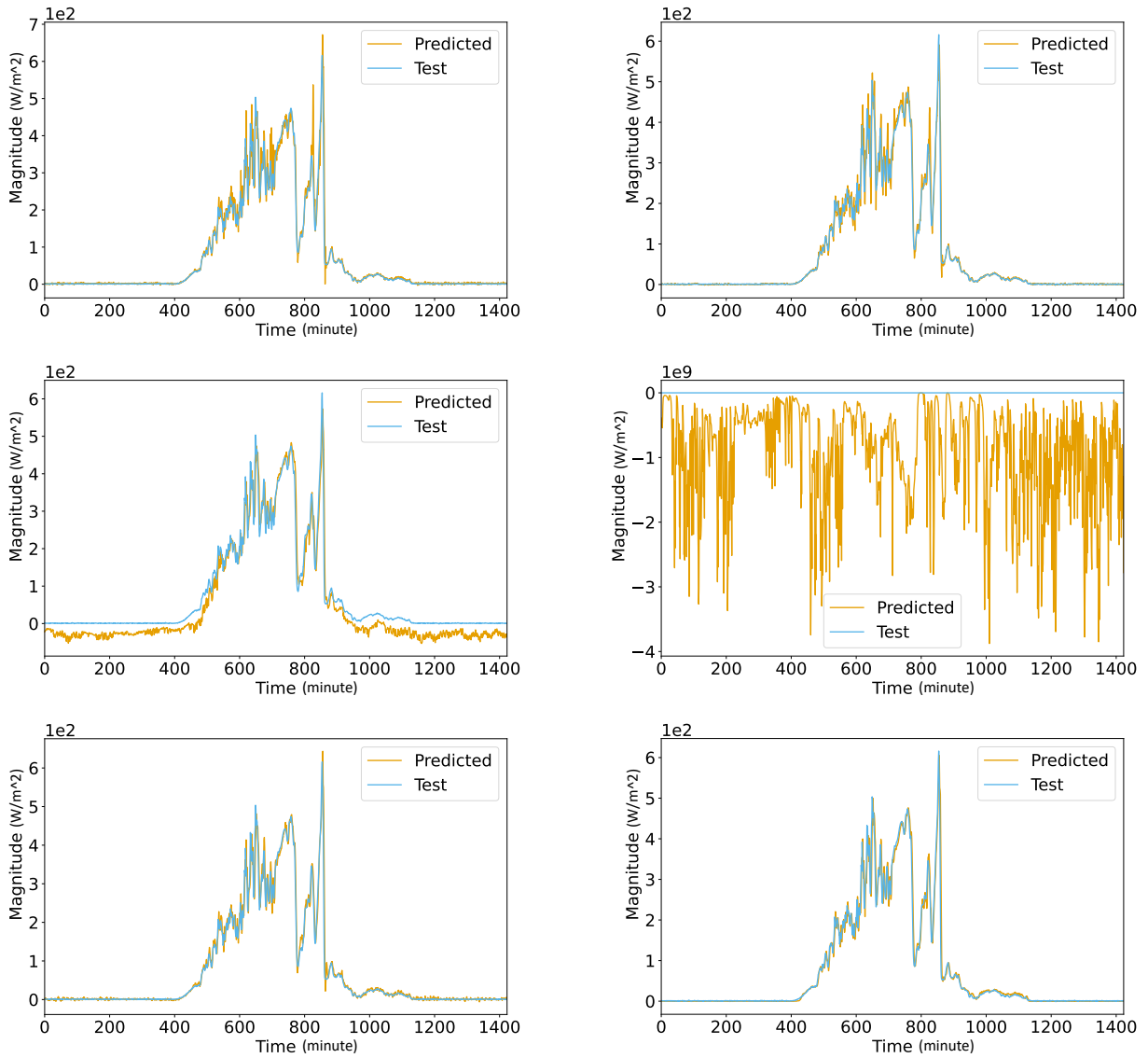


Figure 7: RNN (top left), LSTM (top right), ICRNN (middle left and middle right with neural architecture of (128, 128) and (256, 256) respectively), LRNN (bottom left), and ICLRNN (bottom right) performance on 2023-12-28 for solar irradiance prediction.

List of Tables

1	Parameter values for CSTRs	36
2	Hyperparameters of neural network models for CSTR	37
3	Testing MSE of ICRNN and ICLRNN with respect to increasing hypothesis space .	38
4	Hyperparameters of neural network models for solar irradiance forecasting	39

Parameter	Value Range
T_s	402 K
C_{A_s}	1.95 kmol/m ³
F	5 m ³ /hr
V_L	1 m ³
Q_s	0.0 kJ/hr
T_0	300 K
R	8.314 kJ/kmol K
C_{A0_s}	4 kmol/m ³
ρ_L	1000 kg/m ³
C_p	0.231 kJ/kg K
E	5×10^4 kJ/kmol
k_0	8.46×10^6 m ³ /kmol hr
ΔH	-1.15×10^4 kJ/kmol

Table 1: Parameter values for CSTRs

Table 2: Hyperparameters of neural network models for CSTR

Model	Activation	Inputs	FLOPs
Plain RNN	Tanh	\mathbf{x}_t^\top	27,924
Plain LSTM	Tanh	\mathbf{x}_t^\top	104,468
LRNN	Tanh	\mathbf{x}_t^\top	159,508
ICRNN	ReLU	$\hat{\mathbf{x}}_t = [\mathbf{x}_t^\top, -\mathbf{x}_t^\top]^\top$	79,892
ICLRNN (Ours)	ReLU	$\hat{\mathbf{x}}_t = [\mathbf{x}_t^\top, -\mathbf{x}_t^\top]^\top$	28,436

Table 3: Testing MSE of ICRNN and ICLRNN with respect to increasing hypothesis space

Model Size	Testing MSE		Lipschitz Constant	
	ICRNN	ICLRNN	ICRNN	ICLRNN
(32, 32)	$8.87 \times 10^{-5} \pm 3.964 \times 10^{-7}$	$4.61 \times 10^{-4} \pm 1.899 \times 10^{-4}$	$6.21 \times 10^{-1} \pm 5.547 \times 10^{-3}$	$7.35 \times 10^{-1} \pm 1.148 \times 10^{-1}$
(64, 64)	$9.01 \times 10^{-5} \pm 2.423 \times 10^{-7}$	$1.63 \times 10^{-4} \pm 3.879 \times 10^{-5}$	$6.88 \times 10^{-1} \pm 2.154 \times 10^{-2}$	$7.62 \times 10^{-1} \pm 6.123 \times 10^{-2}$
(128, 128)	$3.92 \times 10^{-4} \pm 6.278 \times 10^{-5}$	$2.89 \times 10^{-4} \pm 8.914 \times 10^{-5}$	$8.96 \times 10^{-1} \pm 2.392 \times 10^{-2}$	$8.24 \times 10^{-1} \pm 4.015 \times 10^{-2}$
(256, 256)	$3.58 \times 10^2 \pm 9.456$	$7.69 \times 10^{-5} \pm 1.891 \times 10^{-6}$	$2.92 \times 10^1 \pm 2.738$	$7.05 \times 10^{-1} \pm 7.269 \times 10^{-3}$
(512, 512)	NaN	$2.25 \times 10^{-4} \pm 2.007 \times 10^{-5}$	NaN	$7.39 \times 10^{-1} \pm 4.494 \times 10^{-2}$

Table 4: Hyperparameters of neural network models for solar irradiance forecasting

Model	Activation	Inputs	FLOPs
Plain RNN	Tanh	\mathbf{x}_t^\top	399,362
Plain LSTM	Tanh	\mathbf{x}_t^\top	1,596,418
LRNN	Tanh	\mathbf{x}_t^\top	1,195,010
ICRNN	ReLU	$\hat{\mathbf{x}}_t = [\mathbf{x}_t^\top, -\mathbf{x}_t^\top]^\top$	2,498,562
ICLRNN (Ours)	ReLU	$\hat{\mathbf{x}}_t = [\mathbf{x}_t^\top, -\mathbf{x}_t^\top]^\top$	401,410